Pt-ligand Single-atom Catalysts: Tuning Activity by Oxide Support Defect Density

Journal:	*Catalysis Science & Technology*
Manuscript ID	CY-ART-12-2019-002594.R1
Article Type:	Paper
Date Submitted by the Author:	11-Apr-2020
Complete List of Authors:	Zhou, Xuemei; Indiana University Bloomington, Dept. of Chemistry Chen, Linxiao; Indiana University Bloomington Sterbinsky, George ; Argonne National Laboratory Mukherjee, Debangshu ; Oak Ridge National Laboratory, Center for Nanophase Materials Sciences Unocic, Raymond; Oak Ridge National Laboratory, Center for Nanophase Materials Sciences Tait, Steven; Indiana University Bloomington, Dept. of Chemistry

Pt-ligand Single-atom Catalysts: Tuning Activity by Oxide Support Defect Density

Xuemei Zhou,[a] *Linxiao Chen,*[a] † *George E. Sterbinsky,*[b] *Debangshu Mukherjee,*[c] *Raymond R. Unocic,*[c] *Steven L. Tait*[a] *

[a] Dr. X. Zhou, Dr. L. Chen, Prof. S. L. Tait, Department of Chemistry, Indiana University, 800 E. Kirkwood Ave., Bloomington, Indiana 47405 (U. S. A.), E-mail: tait@indiana.edu;

[b] Dr. G. E. Sterbinsky, Advanced Photon Source, Argonne National Laboratory, 9700 S. Cass Ave., Lemont, Illinois 60439 (U. S. A.);

[c] Dr. D. Mukherjee, Dr. R. R. Unocic, Center for Nanophase Materials Sciences, Oak Ridge National Laboratory, 1 Bethel Valley Rd, Oak Ridge, TN 37830 (U.S.A.).

† Present address: Institute for Integrated Catalysis, Pacific Northwest National Laboratory, Richland, Washington 99352, USA

Keywords: single-atom platinum; metal oxide surface defects; metal-ligand assembly; hydrosilylation reaction.

Abstract

The support-metal interaction is an important element of heterogeneous catalyst design and is particularly critical for the rapidly growing field of single-atom catalysts (SACs). We investigate the impact of varying the defect density of the titania support on metal-organic Pt SACs for hydrosilylation reactions. Pt SACs are decorated on the powder titania support, employing a metal-ligand interaction with a dipyridyl-tetrazine ligand (DPTZ). The single-atom nature of Pt is verified by X-ray absorption spectroscopy (XAS) on both pristine and defective titania surfaces. These Pt species have a +2 oxidation state and are stabilized by bonding with DPTZ, surface oxygen, and residual chloride from the metal precursor. The catalytic activity is evaluated for the alkene hydrosilylation reaction and it is discovered that the activity of Pt-ligand is positively correlated with the defect density of the titania support. The turnover number (TON) is calculated to be 12 530 for Pt SACs on a defective surface, which is significantly higher than Pt SACs on a pristine titania surface (830) for the same reaction period (10 min) under the same conditions (70 °C). We ascribe the high activity of Pt SACs on defective titania surfaces to two aspects: the coordination of Pt with more chloride than on pristine titania surfaces, which shortens the induction period of the reaction, and the preferential dispersion of Pt-DPTZ units on defective regions of titania surfaces, allowing facile contact between Pt sites and reactants. The supported Pt-DPTZ SACs show high stability through multiple cycles of batch reactions. This work demonstrates an efficient approach to improve the activity and stability of SACs by optimizing the metal-support interaction, which can also be applied to other oxide surfaces to further develop next-generation heterogeneous single-atom catalysts.

Introduction

The metal-support interaction is known to significantly affect the activity of heterogeneous catalysts.[1-4] The strong interactions between Pt metal sites and different oxide supports affect the morphology and composition of the metal species, leading to significant differences in catalytic activity and selectivity for reactions such as Fischer-Tropsch synthesis, CO oxidation, and hydrogenation.[5-10] Noble metal nanoparticles are often encapsulated by the support materials due to these strong inteactions.[5, 11-12]

In recent years, there has been growing interest in noble metal single-atom species to maximize atom-utilization efficiency and take advantage of unique properties of single atoms to enhance selectivity and activity.[13-14] As single atoms, they are more sensitive than nanoparticles to the surrounding interactions from coordination partners, including the support.[3] Therefore, modification of the support surface properties is expected to have a strong impact on the properties of single atoms including coordination environment, electronic properties, nucleation behavior, and surface geometry.[3]

Current methods to synthesize single-atom catalysts (SACs) usually involve wet-chemical approaches, including defect-engineering on oxide surfaces,[15] binding site design on zeolites,[16] impregnation using strong electrostatic adsorption (SEA) at very low concentration of noble metals,[17] alkali-oxo isolated single atoms,[18-20] or single-atom alloys.[18] A surface organometallic chemistry (SOMC) methodology has been adopted to synthesize single atoms as well. The organic ligands can be removed by a thermolytic, nonoxidative procedure after grafting on the surface. A key feature of the SOMC method is the opportunity to create tunable SAC properties, particularly higher reaction selectivity, by tuning the ligand.[21] SOMC is applied to reveal the elementary steps of molecular chemistry. The single transition metal atoms are involved and are covalently or ionically bound to a solid support. Additionally, the metal center is bound with functional ligands and spectator ligands. The functional ligand is formally oxidizing the metal center and becomes an intermediate during the elementary steps, for example metal-(carbene)(hydride). The spectator ligand is not involved during the reaction but plays an important role in tuning the electronic or steric properties of the metal center.[22] The difference between SOMC and the other above-mentioned single atom catalysts (SAC) is that the supported SOMC catalysts keep at least part of the ligands. The ligand thus may control the oxidation state, geometry and d^n electron configuration of the metal center.[22] Well-defined surfaces like oxides, sulfides, carbon or graphene can be used to target specific functionalities on the surfaces, and these supports are usually regarded as a rigid ligand. However, in the SAC studies, the properties of support have shown to impact the functionality of the metal center.[15, 23]

We have developed a metal-organic coordination strategy to synthesize Pt SACs on oxide surfaces.[24] This metal-organic complexation strategy utilizes ligands to tune the charge state of single metal atoms and stabilize the single-atom centers at high loadings, which we initially demonstrated on model supports (single crystal surfaces) in ultra-high vacuum,[25-26] but later adapted to high-surface-area powder oxide supports under ambient conditions.[24] In these metal-ligand SACs, the proximity of the metal center to the support, which allows for chemical spillover of reaction intermediates,[23] makes the supporting materials very important in determining the activity of the catalyst. For example, the Pt SACs using the metal-ligand strategy on ceria (CeO_2) and magnesia (MgO) supports have been shown in a previous study to be active for hydrosilylation reactions,[24, 27] which is an interesting model reaction for examining SAC selectivity because of the challenges in selective C-H functionalization and avoiding isomerization by-products.

Hydrosilylation reactions of olefins are important industrially for silicon chemistry to convert inexpensive hydrocarbon feedstocks into value-added chemicals. These reactions can be applied for the synthesis of coupling agents, reduction of carbonyl groups, modification and cross-linking of polymers, and particularly for organosilicon copolymers.[28-32] Compared to hydrosilylation using homogeneous catalysts, heterogeneous catalysis enables recycling of the catalyst and a straightforward separation of products from reaction suspension. Therefore, considerable efforts have been made to heterogenize hydrosilylation reactions.[33-36] In Maciejewski's work, the heterogeneous catalytic system (Pt supported on a highly hydrophobic styrene–divinylbenzene resin) can be used without significant loss of activity. For supported single-site Pt on Al_2O_3, the catalysts show higher selectivity to products than the Pt nanoparticles, albeit at a high reaction temperature.[34]

Our previous study has shown that the support CeO_2 outperforms MgO with same Pt-DPTZ loading for the hydrosilylation of oct-1-ene, which may be ascribed to the effect of natural surface defects on CeO_2.[24] Therefore, in order to explore the role of surface defects, in this work we employ titania (TiO_2) as supports, where a high degree of control on the TiO_2 surface defects can be introduced.[37] TiO_2 is also environmentally benign, and highly resistant against chemical corrosion.[38-40] The objective of this work is to examine the influence of TiO_2 surface defects on catalytic hydrosilylation performance of metal-organic SACs with the aim to understand how defect tuning can influence SACs and improve catalytic reaction performance.

The density of surface defects, primarily Ti^{3+} / oxygen vacancy (Ov) pairs, is controlled by thermal annealing of the TiO_2 powders before Pt loading and can be characterized by EPR spectroscopy. Pt single-atom with stabilizing tetrazine ligands (3,6-di-2-pyridyl-1,2,4,5-tetrazine, DPTZ, **Figure 1a**) are loaded on these TiO_2 surfaces, then tested for catalytic alkene hydrosilylation activity. The catalyst activity is found to increase with TiO_2 annealing temperature up to 500 °C, indicating a positive correlation of activity with defect density over a range of catalyst treatments. The catalyst can be recovered and reused for several cycles of batch reactions: Pt-DPTZ on defective TiO_2 surfaces is stable for at least four cycles, but supported bare Pt or Pt nanoparticles (no DPTZ ligand) on either pristine TiO_2 or on defective TiO_2 are only active for the first cycle, demonstrating that the presence of the ligand significantly improves the durability of the catalyst under reaction conditions in solution.

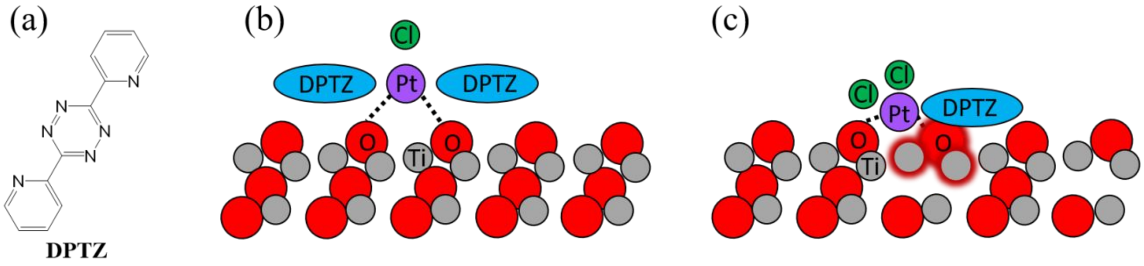

Figure 1. (a) Structure of dipyridyl tetrazine (DPTZ). Schematic illustrations of Pt-DPTZ on (b) pristine TiO_2 (101) and on (c) defective TiO_2 (with oxygen vacancy). The sub-surface oxygen vacancy leads to local electron-rich surface sites,[41-43] which impact the coordination around the Pt center and thus affect the reaction activity, as described in the text.

Experimental

Materials and chemical reagents

Titanium (IV) oxide (anatase, nanopowder, <25 nm, 99.7% trace metals basis), 3,6-di-2-pyridyl-1,2,4,5-tetrazine (DPTZ, 96%), dihydrogen hexachloroplatinate (IV) hexahydrate (99.95%, $H_2PtCl_6•6H_2O$), and decane (99%) were purchased from Sigma-Aldrich. 1-Butanol and dichloromethane (DCM) were purchased from VWR Chemicals. Toluene was purchased from Macron. Dimethoxymethylsilane (97%) and 1-octene (97%) were purchased from Alfa Aesar. All chemicals were used without further purification.

Catalyst preparation

Titania was used as the catalyst support, either in its pristine form (as received) or by applying an annealing treatment at a specific temperature to generate oxygen vacancy (Ov) surface defects. For the annealed TiO_2 supports, 0.4 g TiO_2 powder was loaded in a ceramic crucible and placed into the center of a tube furnace. The tube furnace was first purged with pure lab nitrogen gas for 30 min, then a flow of forming gas (5 vol. % hydrogen, balanced in nitrogen gas, Airgas, 99.99%) at 2 L/h was started. Under this gas flow, the temperature was increased from room temperature to the desired annealing temperature at a ramp rate of 10 °C/min. After holding at a fixed temperature for 1 h, the furnace was cooled down to room temperature in the forming gas flow. Annealing treatments under hydrogen gas have been shown to create defects in the surface and sub-surface.[15, 44-45] It is important to note that while Ov sites created in UHV by Ar^+ or electron beam irradiation have been demonstrated to have a significant degree of mobility[46] and to be unstable in air,[47-48] Ov generated by hydrogen treatment have been shown to be stabilized by the presence of bound hydrogen.[49-50] As shown in prior studies, near-surface oxygen vacancies produce electron-rich surface sites (**Figure 1c**).[41-43]

The synthesis of single-atom Pt on TiO_2 is based on a metal-organic wet impregnation method that has been previously reported by our group.[24] Briefly, 0.3 g TiO_2 powder (pristine or annealed, as described in the preceding paragraph) was dispersed in 1-butanol, sonicated for 1 min, then stirred for 30 min. DPTZ was dissolved in 1-butanol to form a pink solution. Then, 0.0080 g $H_2PtCl_6•6H_2O$ (1 wt% by Pt; dissolved in 5 mL 1-butanol) and the pink DPTZ solution were added in sequence into the TiO_2/1-butanol. After stirring overnight, the suspension was dried under an air stream. The dry precipitate was collected and washed using de-ionized water. DCM was used to clean the sample at the last step to remove residual DPTZ from the surface. Afterwards, the final filtered powder was collected and dried in air. For the reference samples of bare Pt only (no DPTZ), the same procedure was used, except for the omission of the DPTZ solution. In the Pt nanoparticle preparation, 1 mL of 0.1 M NaOH aqueous solution was added into TiO_2 suspension before the addition of Pt-precursor (1 wt% by Pt). After precipitation, the suspension was dried at 100 °C in oven and then reduced in hydrogen (balanced with 50% Ar) at 400 °C for 1 h.

Hydrosilylation reaction

The hydrosilylation reaction between 1-octene and dimethoxymethylsilane was performed in a closed reaction tube. The reaction solution consists of 2.3 mmol dimethoxymethylsilane and 3.1 mmol 1-octene dissolved in 1.5 mL toluene. Catalyst powder was added into the reaction solution once it reached the target reaction temperature (40 °C to 70 °C). The suspension was sampled in 100 μL aliquots at various time intervals (0 min, 5 min, 10 min, 20 min, 30 min) to obtain a yield-time curve. The sampled suspensions were diluted into 10 mL toluene and analyzed by GC-MS for the yield of products and conversion of reactants. Decane (1.1 mmol) is used as a standard reagent for calibration of GC-MS signal response. In each experiment, 5.0-5.2 mg catalyst was used, and the Pt concentration is in the range of 5-15 ppm.

Cyclic batch reaction experiments were performed under the same experimental conditions as above. After each cycle at 70 °C for 30 min, the reaction mixtures were then separated from the solid catalysts after the catalyst deposited at the bottom of the reactor. The catalysts were further cleaned with 1 mL toluene to wash out the adsorbed reactants or products. A fresh reaction mixture at the similar equivalent was added into the same reactor which contains solid catalyst. The change of reactants and products were sampled and measured by GC-MS. The cycles were repeated for 5 times for Pt-DPTZ/TiO_2 500 °C and 3 times for bare Pt supported on TiO_2 (pristine and defective) without DPTZ presence.

For XPS or ICP-MS analysis, the solid catalysts were collected and cleaned after first and third cycle of hydrosilylation reaction. A certain amount of the recycled solid catalysts was treated in aqua regia at 70 °C for 1 h and the supernatant was collected for ICP-MS analysis to quantify the Pt amount. The rest of the collected solid powers after reaction were analyzed by XPS for elemental compositions.

Blank experiment using only TiO_2 was performed to eliminate the experimental error. Catalytic experiments were repeated several times and results were reproducible.

Characterization

X-ray photoelectron spectroscopy (XPS) measurements were conducted at room temperature with a PHI Versaprobe II XP spectrometer using a monochromated Al Kα X-ray source. N 1*s*, C 1*s*, O 1*s*, Pt 4*f*, and Ti 2*p* spectra were measured for all samples. Additionally, Cl 2*p* spectra were measured for all Pt-loaded samples. A Pt *4f* region was collected for clean TiO_2 as a background to subtract from other spectra. A binding energy (BE) correction was made using the Ti $2p_{3/2}$ peak (458.0 eV) for all samples. The DPTZ loading was quantified using the area ratio between the N 1*s* peak and Pt 4*f* peak (Table 1). XPS peak fitting was performed using CasaXPS software using the same full width at half maximum value for each component in the same region. The separation of $4f_{7/2}$ and $4f_{5/2}$ was fixed to be 3.2 eV.

EPR spectra were acquired using a Bruker EMX X-band EPR spectrometer at room temperature, microwave frequency of 9.866 GHz, microwave attenuator at 15.0 dB, microwave power of 6.38 mW, modulation frequency of 100 kHz, and modulation amplitude of 4.0 G. X-ray diffraction (XRD) measurements were recorded with a Panalytical Empyrean Diffractometer equipped with a Cu Kα (λ= 0.154 nm) X-ray source and a transmission-reflection spinner. The scanning range was set from 20° to 85°, with a step of 0.02°/s. Raman spectra were acquired on Renishaw 1000B microRaman instrument equipped with a Coherent Innova 70-2 Ar^+ laser with emission at 514 nm.

Samples for electron microscopy were prepared by drop-casting Pt-DPTZ on TiO_2 particles dispersed in ethanol onto lacey carbon TEM grids. STEM-EELS measurements were performed using a probe aberration-corrected NION UltraSTEM 100, operated at 60 kV. HAADF-STEM images were collected using an annular dark field detector with a convergence angle of 31 mrad and collection angles between 84-200 mrad at over a 20 nm × 20 nm field of view. EELS measurements were performed with a 3 μm aperture, using a dispersion of 0.3 eV per channel and a scanning pixel dwell time of 0.1 s per pixel. The acquired spectra were then corrected for noise using local background averaging,[51] with the background averaged in the vicinity of a scan pixel with a 3 pixel standard deviation gaussian. Transmission electron microscopy (TEM) analysis was performed on JEOL JEM 1400plus, which is operated at 120 kV.

X-ray absorption spectroscopy (XAS) measurements were performed at the 9-BM beamline at the Advanced Photon Source of Argonne National Laboratory. The solid sample was pressed into a pellet with diameter of 7 mm and fixed to a mobile sample holder. The monochromatized X-ray energy was calibrated with the Pt L_3-edge (11563.7 eV). X-ray absorption spectra were measured at the Pt L_3-edge, from to 11 363 to 12 365 eV. Both fluorescence and transmission data were collected and share similar features; fluorescence data have better signal to noise ratio and were used for analysis. XAS of a Pt foil, an PtO_2 pellet, and a K_2PtCl_6 pellet were measured as standard references for XANES of Pt(0) and Pt(+4) in different coordination environments. Reference samples were measured in transmission mode due to their high concentration. Fitting of EXAFS spectra was performed using Artemis software.[52] Pt-N and Pt-Cl paths were selected from Pt(2+)(pyridine)$_2$Cl$_2$ structure, where R_{eff}(Pt-N)=1.996 Å and R_{eff}(Pt-Cl)=2.293 Å. Pt-O path was selected from PtO_2 structure, where R_{eff}(Pt-O)=2.070 Å. The S_o^2 and ΔE_0 were defined by fitting the standard samples. For example, the S_o^2 and ΔE_0 is simulated to be 0.9 and 9.0 respectively for Pt-Cl path, by fitting the K_2PtCl_6 sample. The S_o^2 and ΔE_0 is simulated to be 0.9 and 9.8 respectively for Pt-O path, by fitting the PtO_2 sample. The S_o^2 and ΔE_0 is simulated to be 1.2 and 9.8 respectively for Pt-N path, by fitting the PtO_2 sample using Pt-N path.

CO adsorption experiments were performed with a diffuse reflectance IR environmental chamber (PIKE Technologies, 162-4160, HTV) at room temperature (25 °C). Background spectra were collected under Ar flow before purging the chamber with 10% CO in Ar. After CO flowed into the chamber for 15 min, the diffuse reflectance infrared Fourier transform spectra (DRIFTS) were collected with a Magna 550 FTIR spectrometer (Nicolet). Each DRIFT spectrum was an average of 500 scans and was converted into Kubelka-Munk units. Afterwards, the chamber was purged with pure Ar for 15 min to remove gas phase CO, as well as weakly adsorbed CO from the catalyst surface.

In order to quantitatively determine Pt loading, ICP-MS measurements were performed with an Agilent 7700 quadrupole ICP-MS instrument. Solid catalysts were treated with aqua regia to dissolve all Pt. The calibration curve was determined using Platinum Standard for ICP (Sigma-Aldrich, TraceCERT, 1000 mg/L Pt in hydrochloric acids) diluted with trace-free HCl to a range of concentrations.

Results and Discussion

TiO_2 Characterization

We prepared a set of TiO_2 support powders using a range of annealing temperatures from 300 °C to 500 °C, which has been shown to produce a range of surface defect densities.[15, 45, 53] The formation of Ti^{3+}/ O_v (oxygen vacancy) states in TiO_2 introduced by annealing treatment is characterized by continuous wave (CW) electron paramagnetic resonance (EPR) spectroscopy, which is widely used in the characterization of paramagnetic centers.[54-57] The CW-EPR technique provides signals based on the g tensor only, which could be used to distinguish single electrons trapped in regular lattice sites, interstitial sites, or defective sites.[54, 58] Pristine anatase shows only a weak signal at g-tensor value of approx. 2.00 (**Figure 2a**), due to Ti^{3+}/O_v naturally present in commercial anatase,[59-60] although our spectral features are broader than in those studies because acquisition was done at room temperature.[61] For anatase powder annealed from 300 °C to 500 °C, a clear increase in intensity of this signal ($g \approx 2.00$) can be observed reaching a three-fold increase for anatase annealed at 500 °C, indicating a higher concentration of Ti^{3+}/O_v sites, which are introduced by annealing in H_2/N_2.[15, 60, 62] Raman spectroscopy shows a blue shift of all five modes for anatase annealed at 400 °C and 500 °C (**Figure S1a**), indicating shortening of the correlation length because of the presence of oxygen vacancies.[47] The material turns from white pristine anatase to a yellow color after annealing at 500 °C (**Figure S1a,** inset). However, annealing TiO_2 above 500 °C leads to EPR signal attenuation (**Figure 2a**)[15] and changes in Raman spectra (**Figure S1a**) and XRD patterns (**Figure S1b**) that are all consistent with a transition to rutile TiO_2. The

XRD results also indicate that the particles sinter significantly above 500 °C (crystallite size increases from 17.1 nm to 156.4 nm, **Table S1)**.

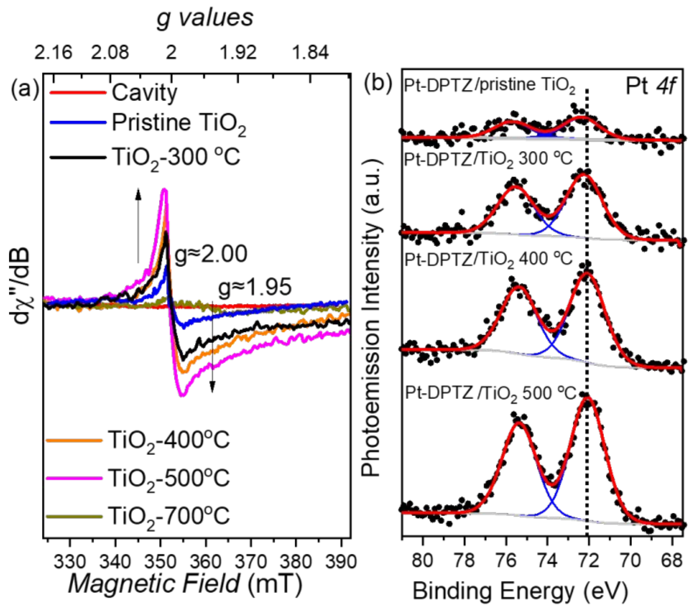

Figure 2. (a) Solid-state EPR spectra for pristine TiO_2 (blue), and for various degrees of defective TiO_2 prepared by annealing at 300 °C, 400 °C, 500 °C, and 700 °C for 1 h in H_2/N_2. Blank cavity reference shown in red. (b) Pt *4f* XP spectra for Pt-DPTZ SACs on pristine TiO_2 and on defective TiO_2, annealed at 300 °C, 400 °C, and 500 °C before catalyst loading. XPS data are shown as black dots with fitting components (blue) and envelope (red) as solid lines.

Pt-DPTZ/TiO_2 Characterization

The pristine TiO_2 or the defective TiO_2 is used as the support to load Pt with DPTZ (**Figure 1b-c**) using a one-step impregnation method.[24] The chemical states and coordination of Pt with ligand on various defective TiO_2 supports are examined by XPS (**Figure 2b**, **Figure S2-S3**). Pt *4f* peaks in **Figure 2b** show that the Pt that is supported on

TiO_2 with DPTZ is predominantly in a +2 oxidation state (Pt $4f_{7/2}$ BE at 72.1 eV, consistent with prior studies on Au(100) and TiO_2 surfaces[26, 63-64]). The increased defect density on the TiO_2 support (increased annealing temperature) leads to a significant increase in Pt loading under the same synthesis conditions, as shown by the intensity increase of Pt 4*f* XPS (**Figure 2b and Table 1**) and by ICP-MS analysis (**Table S2**).

Table 1. Catalyst composition as number ratios based on XPS measurements. XPS peak areas are corrected by sensitivity factors to calculate DPTZ/Pt, Pt/Ti, and Cl/Pt number ratios.

	DPTZ/Pt	Pt/Ti (10^{-3})	Cl/Pt
Pt-DPTZ/Pristine TiO_2	0.92	1.6	0.57
Pt-DPTZ/TiO_2 300 °C	0.53	4.5	0.58
Pt-DPTZ/TiO_2 400 °C	0.39	4.5	0.73
Pt-DPTZ/TiO_2 500 °C	0.38	6.4	1.37
Pt-DPTZ/TiO_2 700 °C	0.34	38.4	0.88
Pt/Pristine TiO_2	-	1.8	*
Pt/TiO_2 500 °C	-	1.7	*
Pt NPs/Pristine TiO_2	-	3.8	0.60
Pt NPs/TiO_2 500 °C	-	3.1	0.95

*indicates the Cl detection is below 0.02 at.%.

To verify the single-atom nature and to reveal the local coordination environment of the Pt centers, X-ray absorption near edge structure (XANES) and extended X-ray absorption fine structure (EXAFS) (**Figures 3** and **4**) measurements were performed for Pt-DPTZ SACs on different TiO_2 surfaces. The XANES spectra at the Pt L_3-edge from Pt-DPTZ SACs/pristine TiO_2 (**Figure 3)** show white line peaks with intensity indicative of the presence of oxidized platinum species (between zero to +4 states), in agreement with the XPS results.

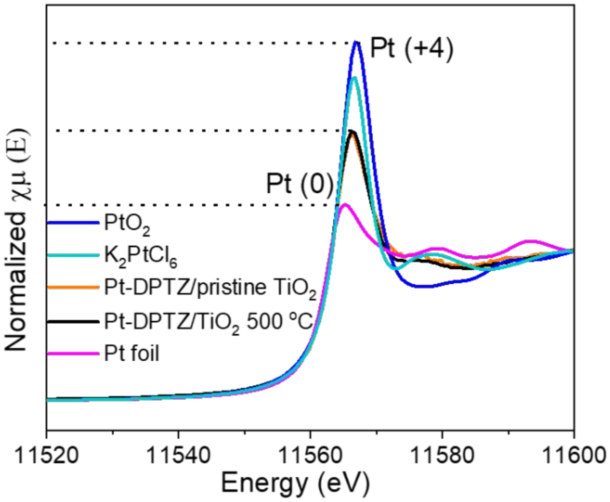

Figure 3. Pt L_3 edge XANES for Pt SACs with DPTZ on pristine TiO_2, on defective TiO_2, Pt foil, commercial PtO_2, and K_2PtCl_6. The Pt-DPTZ (orange and black color) white line intensity indicates an intermediate oxidation state between 0 and +4.

EXAFS measurements at the Pt L_3 edge provide information about the local coordination environment of Pt. For Pt-DPTZ on either pristine TiO_2 (**Figure 4a**) or on defective TiO_2 (**Figure 4b**), we see no indication of Pt-Pt coordination (compare to Pt foil in **Figure 4g**). These results demonstrate the single-atom nature of platinum on the pristine TiO_2 and defective TiO_2 surfaces with DPTZ. Previous reports show that even for clusters < 10 atoms, Fourier transform EXAF spectra do show a Pt-Pt path intensity,[65] which is different from the current EXAF spectra. However, it should be noted that while we do not observe a Pt-O-Pt path in our data, small, oxidized Pt particles with no long-range order may not produce a well-defined EXAFS signal and thus cannot be excluded as a possible minority species on the catalysts.[66] Therefore, the distribution of the supported single Pt-ligand catalysts is further characterized by high-resolution electron microscopy (**Figure 5**).[67]

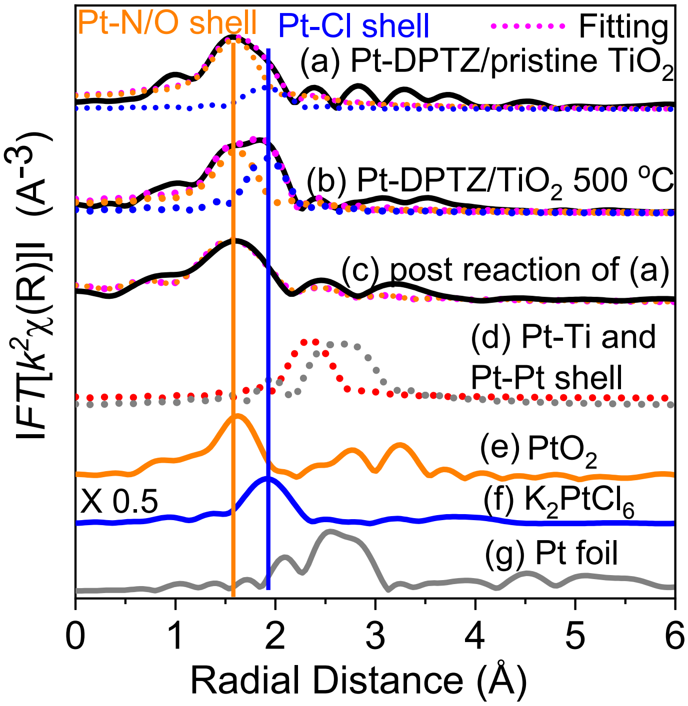

Figure 4. Fourier transforms of k^2-weighted Pt L_3 edge EXAFS data and their fitting results in the first shell. Pt-DPTZ on (a) pristine TiO_2 and (b) on defective TiO_2 annealed at 500 °C. Spectrum (c) is the sample of (a) after reaction. The fitting shown in this graph was obtained using Pt–N (yellow dash) and Pt–Cl (blue dash) paths, assuming $S_o^2 = 1.2$, ΔE_0 is 9.8 eV for Pt-N shell, and $S_o^2 = 0.9$, ΔE_0 is 9.0 eV for Pt-Cl shell. Reference samples (e) PtO_2, (f) K_2PtCl_6 and (g) Pt foil are also shown. These EXAF spectra were acquired simultaneously with the XANE spectra in **Figure 3**. (d) The Pt-Pt (red dash) and Pt-Ti (grey dash) paths are shown for comparison. Values for independent fitting parameters and k ranges for Fourier transformation are given in **Table S3**, as well as an alternative fitting model with Pt-O and Pt-Cl paths.

HAADF-STEM with spherical-aberration correction demonstrates that the Pt species with DPTZ are well dispersed on the defective TiO_2 surface (Pt-DPTZ/TiO_2 500 °C, **Figures 5a-5c**) as well as on the pristine TiO_2 surface (**Figure 5d**). **Figure 5c** shows these Pt are mainly isolated single-atom Pt, likely separated by DPTZ. Without the presence of DPTZ, the Pt aggregates and forms nanoparticles about 2 nm in size on the pristine TiO_2 surface (**Figure 5e**). However, when Pt is dispersed on defective TiO_2 (500 °C anneal), no clear Pt metal nanoparticles are observed and the Pt preferentially locate in line with Ti rows (**Figure 5f**).[68]

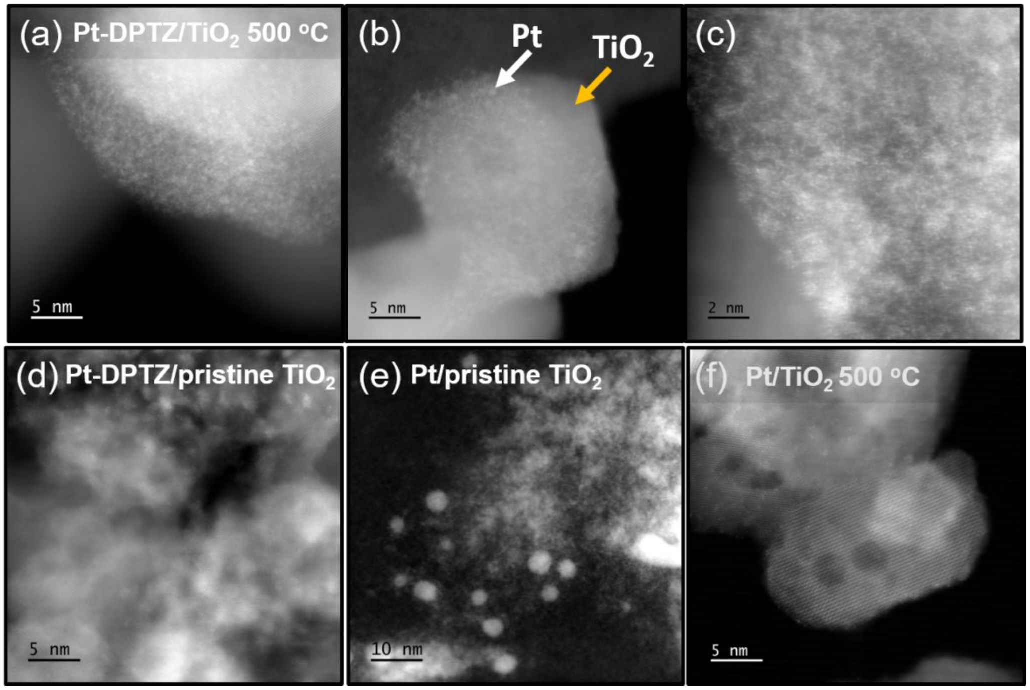

Figure 5. HAADF-STEM images for (a-c) Pt-DPTZ/TiO_2 500 °C, (d) Pt-DPTZ/pristine TiO_2, (e) Pt/pristine TiO_2 (without ligand) and (f) Pt/TiO_2 500 °C (without ligand).

Hydrosilylation Reaction

The catalytic performance of these Pt-DPTZ SACs on defective TiO_2 supports was evaluated for the hydrosilylation of 1-octene with dimethoxymethysilane (**Scheme 1**). The anti-Markovnikov addition product, dimethoxy(methyl)octylsilane, is detected by gas chromatography−mass spectrometry (GC−MS).

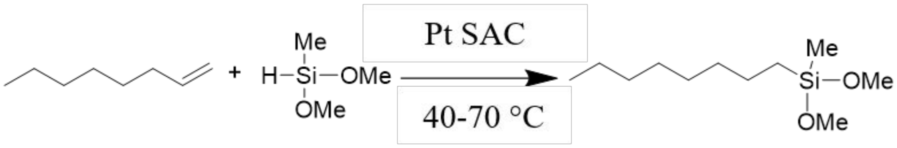

Scheme 1. Hydrosilylation reaction of 1-octene with dimethoxymethysilane to produce dimethoxy(methyl)octylsilane.

We compared a series of catalysts on different TiO_2 supports to evaluate activity for hydrosilylation at 70 °C (**Figure 6a**). After 30 min of reaction, less than 5% yield of product is detected using Pt-DPTZ SACs on pristine TiO_2 as well as the Pt-DPTZ on the TiO_2 support annealed at 300 °C. A much more significant increase is observed for TiO_2 supports annealed at 400 °C or 500 °C, which both show complete conversion under these conditions. We find the reaction reaches 100% conversion of silane and close to 100% yield of product for the most active catalyst (Pt-DPTZ/TiO_2 500 °C) at 70 °C after 10 min (**Figure 6a**). The reaction yields are generally below 100% due to side reactions, for example, dimerization of the silane product.[27] An excess (1.3 eq.) of 1-octene was used to avoid limiting reaction yield due to isomerization and hydrogenation of 1-octene. The Pt-DPTZ on TiO_2 annealed at 700 °C gives a product yield less than 10%, indicating that perhaps some new type of inactive defect site is created at this annealing pre-treatment condition (this is coincident with the transition to rutile, but that transition is not expected to inherently alter the surface sites). The trend in increasing activity up to 500 °C follows a trend similar to the increase of defects detected by EPR. The TON is given in **Table S2**, calculated at 10 min reaction time, which shows for the most active sample, turnover number of 12 530 is obtained. When only TiO_2 (500 °C anneal) is used without Pt ("blank" in **Figure 6a**), the catalyst is not active.

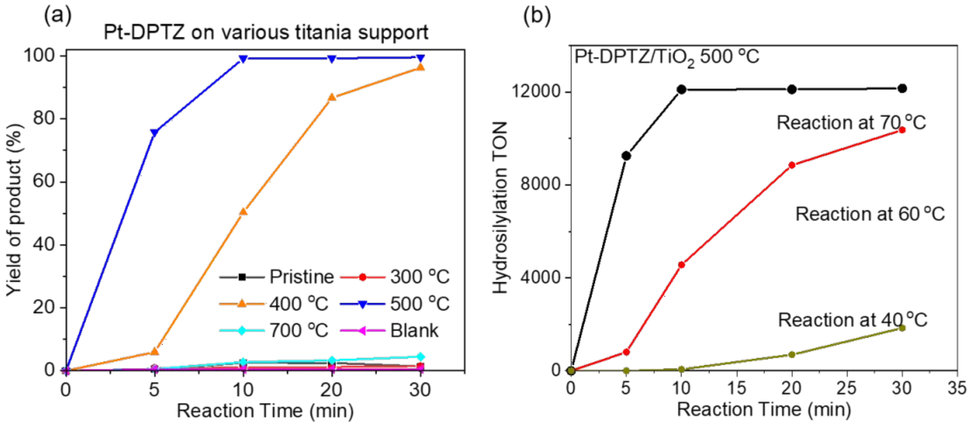

Figure 6. (a) Product yield of hydrosilylation reaction at 70 °C for five Pt-DPTZ SACs on different TiO_2 supports. The blank experiment is performed using TiO_2 (500 °C anneal) only and shows no product yield. (b) Catalytic performance shown as turn-over number (TON = mol product/mol Pt) during 30 min of reaction time for Pt-DPTZ SACs on TiO_2 annealed at 500 °C at reaction temperatures of 40 °C, 60 °C, and 70 °C.

For Pt-DPTZ SACs loaded on TiO_2-annealed at 500 °C (Pt-DPTZ/TiO_2 500 °C), the reaction starts immediately and in 10 min the reaction is complete. However, for Pt-DPTZ SACs loaded on TiO_2-annealed at 400 °C (Pt-DPTZ/TiO_2 400 °C), generation of product reaches a full conversion of silane after 30 min. The induction period for Pt SACs on a pristine TiO_2 surface or TiO_2 annealed at 700℃, is much longer, so that only a small fraction of product is formed in this reaction period. The differences in the support structure have a significant impact on the induction period and activity of the catalyst

The Pt-DPTZ/TiO_2 500 °C catalyst at 70 °C after 30 min shows a reaction yield (99.5%) higher than that of the Karstedt catalyst (86%, measured in our experiments[24]). This catalyst also shows a TON at 10 min (70 °C) that is comparable to single Pt-DPTZ catalysts on CeO_2[27] and significantly better than Pt-DPTZ SAC on MgO[27] or than other Pt SACs on TiO_2.[36] To explore the activity of the most active catalyst (Pt-DPTZ/TiO_2 500 °C), TON-time profiles were obtained at lower reaction temperatures (40 °C and 60°C, **Figure 6b**) that still allow significant conversion. The activation energy is calculated according to the Eyring Equation[28] **(Figure S5**) to be 134.2 ± 10.4 kJ/mol for the Pt-DPTZ/TiO_2 500 °C catalyst. Activation energy was not calculated for the other catalysts because of experimental temperature range limits to have sufficiently high activity for a reliable calculation at a low enough temperature to avoid toluene evaporation.

Pt-DPTZ SAC Coordination Environment

Following the reaction mechanism proposed by Chalk and Harrod,[28, 69-70] the reaction consists of four elemental steps: oxidative addition of the hydrosilane, coordination of the olefin, migratory insertion of the olefin into the Pt−H bond, and reductive elimination of the hydrosilylation product. To understand how the coordination site of Pt affects the reaction steps, we performed CO adsorption and EXAFS analysis on the supported Pt-DPTZ.

CO adsorption can be used to distinguish isolated, coordinatively-unsaturated Pt single-atoms from larger clusters (**Figure 7**).[17, 71,72] Under our experimental conditions (room temperature, ambient pressure, 10% CO balanced in Ar), no CO adsorption on pristine or defective TiO_2 surface is observed (not shown here). With the loading of Pt-DPTZ SACs on pristine TiO_2, CO adsorption peak on any Pt species is not observed (**Figure 7**, pink), which indicates that Pt is well-coordinated, leaving no open sites to CO. However, a CO adsorption peak in the range of 2080 ~ 2120 cm^{-1} is observed for Pt-DPTZ on defective TiO_2 (500 °C), indicating coordinatively unsaturated Pt sites (**Figure 7**, red). Generally, peaks above 2100 cm^{-1} are ascribed to a stretching band of linearly absorbed CO on a cationic Pt species (Pt coordinated with oxidizing ligands, oxidized Pt clusters, or isolated Pt species).[17, 71, 73] The small peak shoulder at 2093 cm^{-1} (**Figure 7**, red) is likely due to CO adsorption on cationic Pt in oxygen vacancy sites because this matches very well with CO adsorbed on Pt (no ligand) on defective TiO_2 (**Figure 7**, blue). As noted above, there may be a small minority species of clusters on the surface (below EXAFS detection limit) and these may also contribute to CO intensity at 2093 cm^{-1}.

In contrast, when Pt is loaded on the pristine TiO_2 surface without DPTZ (**Figure 7**, black), two dominant peaks are observed. The peak at lower frequency (2080 cm^{-1} to 2020 cm^{-1}) can be ascribed to the Pt metal clusters on the pristine support.[17] There is a minority feature at 2093 cm^{-1}, similar to the shoulder noted above for the Pt-DPTZ spectrum, which is due to CO adsorption on cationic Pt in the small concentration of native oxygen vacancy sites on this support.

The unsaturation in coordination of Pt-DPTZ on defective TiO_2 compared to on pristine TiO_2 is supported by XPS and EXAFS. XPS results in **Table 1** show the DPTZ/Pt ratio drops significantly with support annealing pre-treatment temperature, up to 500 °C annealing temperature: DPTZ/Pt ratio decreases from 0.92 for Pt-DPTZ SACs on pristine TiO_2 to 0.38 for Pt-DPTZ SACs on TiO_2 treated at 500 °C. Conversely, the Cl/Pt ratio increases with defect density on the TiO_2 surface from 0.57 for Pt-DPTZ SACs on pristine TiO_2 to 1.37 for Pt-DPTZ SACs on TiO_2 annealed at 500 °C.

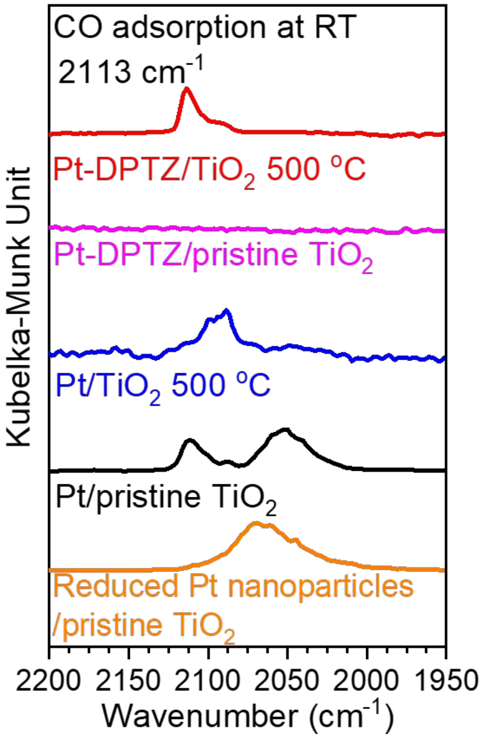

Figure 7. IR spectra of CO adsorption at room temperature (RT) using DRIFTS cell. From top to bottom: Pt- DPTZ on defective TiO_2 (500 °C), Pt-DPTZ on pristine TiO_2, Pt on defective TiO_2, Pt on pristine TiO_2, Pt nanoparticles pre-reduced in hydrogen on pristine TiO_2. No CO adsorption is observed on pristine or defective TiO_2.

The differences in Pt coordination on different TiO_2 supports is corroborated by EXAFS results (**Table 2**). The fit model includes Pt–N/O and Pt–Cl paths, which contribute to the R = 1.56 Å and 1.89 Å features, respectively. The coordination number of Pt–Cl, N (Pt–Cl), is fixed based on XPS analysis of each sample to reduce the number of independent parameters. The fitting models with all independent values are presented for comparison in **Table S3**. *R* (Pt–N/O) = 2.03 Å is between the Pt–N distance (1.996 Å) and Pt–O distance (2.070 Å for PtO_2, and 2.037 Å for $((NH_3)_2PtOH)_2(NO_3)_2)$), which suggests the EXAFS has contributions from both Pt–N and Pt–O paths, indicating Pt-DPTZ coordination and Pt interaction with surface oxygen. The coordination number of Pt with nitrogen/oxygen from the fitting is 4.7 for Pt SACs on pristine TiO_2 and 3.2 for Pt SACs on defective TiO_2, which suggests that on the pristine TiO_2 surface, Pt species are more coordination saturated. An alternate fit model to include a Pt-Pt path was tested, but did not indicate Pt-Pt coordination (**Table S4**).

Table 2. Coordination number EXAFS fitting parameters for Pt-DPTZ on pristine TiO_2 and on TiO_2 annealed at 500 °C, as well as Pt-DPTZ on pristine TiO_2 after hydrosilylation reaction (**Figures 4a**, **4b**, and **4c**, respectively). The *N* (Pt-Cl) value, when set as a free fitting parameter, is close to the measured Cl/Pt ratio in XPS, so it was fixed at that value in the final fitting. More fitting parameters and details about fitting are in **Table S3**.

Fitting parameter/catalysts	*N* (Pt-Cl)	*N* (Pt-N/O)
Pt-DPTZ/pristine TiO_2	0.6	4.7 (± 0.9)
Pt-DPTZ/TiO_2 500 °C	1.4	3.2 (± 0.4)
Pt-DPTZ/pristine TiO_2 (post reaction)	–*	5.2 (± 0.9)

* No significant Pt-Cl detected (see note on **Table S3**).

The STEM images in **Figure 5** and EELS analysis in **Figure 8** investigate the role of surface defects on the coordination of Pt SACs on individual TiO_2 nanoparticles and reveal that the TiO_2 structure is not uniform. Most of the TiO_2 surface does not exhibit an ordered structure in STEM images, but there are some local regions that are crystalline (*e.g.*, upper right region of particle in **Figure 5b**). We observe that the Pt features in Pt-DPTZ samples on defective TiO_2 are predominantly located at disordered regions of the TiO_2 surface. Regions of the surface that are crystalline TiO_2 have almost no Pt features (**Figures 5a-5b**). EELS mapping of the local carbon and Ti concentration indicates a correlation of the DPTZ location with the less-ordered TiO_2 regions (**Figures 8** and **S10**). The carbon and titanium intensity overlay in **Figure 8b** shows that the pristine region (atomic rows visible in **Figure 8a**) has relatively little C intensity. The difference is also apparent when looking at EELS point spectra (**Figure 8c**): in the crystalline region (point 2, **Figure 8a**), we observe a significantly stronger Ti L-edge intensity than in the defective TiO_2 region (point 1). Results in **Figures 5** and **8** thus point to a picture where the defective TiO_2 region is associated with higher concentrations of Pt-DPTZ. Previous investigations on defective TiO_2 have demonstrated the formation of a Ti^{3+}-rich amorphous shell around defective anatase surfaces.[44] Therefore, the preferential distribution of Pt-DPTZ on defective regions of the TiO_2 surface may be due to a strong interaction with the Ti^{3+} sites. This phenomenon is in line with the observation for the bare Pt on defective TiO_2, where Pt preferentially locate at the oxygen vacancy sites (**Figure 5f**).

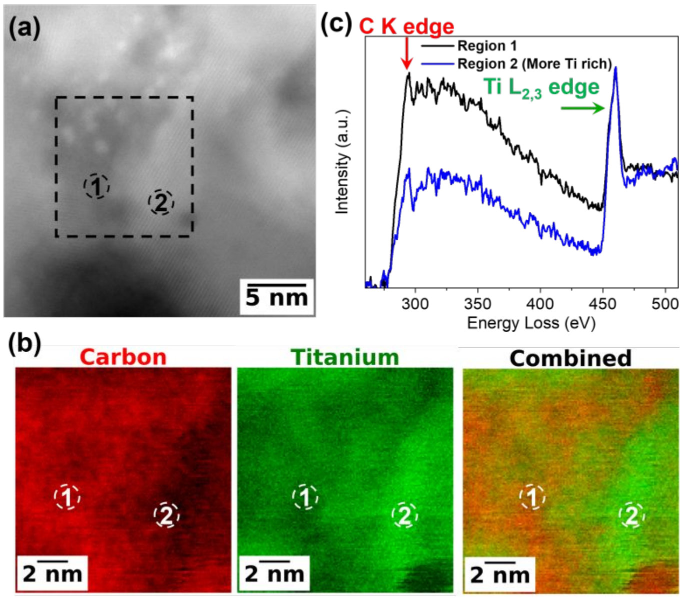

Figure 8. (a) HAADF-STEM Image after EELS analysis, with the black dashed box showing the region on which EELS elemental analysis was performed. (b) Elemental maps for carbon (in red), titanium (in green) from the region marked by the black dashed box in (a). (c) EELS spectra from the point marked as 1 and 2 in (a), showing the presence of both carbon and titanium. A significantly lower intensity of carbon at point 2 is observed as compared to point 1. Note that the large white dots in (a) are due to beam damage during long-time EELS mapping, where the high energy electron beam likely damages DPTZ and induces Pt aggregation (see **Figures 5a-5c** for images before EELS mapping). Further EELS mapping is shown in **Figure S10**.

Therefore, we ascribe the overall high activity to oxygen vacancies on the TiO_2 support changing the coordination environment of Pt single-atoms of the Pt-DPTZ SAC catalysts. The most active Pt SAC shows the lowest DPTZ/Pt ratio, highest Cl/Pt ratio, and least saturated overall coordination environment (**Table 1, Figure 6a, and Table S2**). This specific coordination of Pt SACs on TiO_2 (treated at 500 °C) allows a facile removal of Cl to shorten the induction period. Composition values from XPS for samples after hydrosilylation reaction are presented in **Table 3**. For both Pt-DPTZ on pristine TiO_2 surface and on defective TiO_2 surfaces, an obvious loss of Cl is observed but the DPTZ/Pt ratio is relatively unchanged after one cycle. Those results agree with the EXAFS results: *N* (Pt-Cl) decreases and *N* (Pt-N) is unchanged after the reaction (**Table 2**). Thus, Cl removal during the early stage of the reaction allows higher activity for the Pt-DPTZ / TiO_2 (500 °C) catalyst. There is very little change in XANES spectra white line intensity (**Figure S7**) and almost no change in XPS Pt 4*f* binding energy (**Figure S8c**), which both indicate that the oxidation state of Pt after the hydrosilylation reaction is virtually unchanged.

Table 3. Elemental analysis ratios based on XPS measurements for the DPTZ/Pt, Pt/Ti, and Cl/Pt number ratios for catalysts after cycles of batch reaction.

		DPTZ/Pt	Pt/Ti (10^{-3})	Cl/Pt
Pt-DPTZ/pristine TiO_2	Fresh	0.92	1.6	0.57
	1 cycle	0.93	1.6	0.28
	3 cycles	0.86	1.7	*
Pt-DPTZ/TiO_2 500 °C	Fresh	0.38	6.4	1.37
	1 cycle	0.39	5.9	0.55
	3 cycles	0.40	6.4	*
Pt/TiO_2 500 °C	Fresh	-	1.7	*
	1 cycle	-	*	*
	3 cycle	-	*	*
Pt/pristine TiO_2	Fresh	-	1.8	*
	1 cycle	-	*	*
	3 cycle	-	*	*
Pt NPs/TiO_2 500 °C	Fresh	-	3.1	0.95
	1 cycle	-	2.6	8.36†
Pt NPs/pristine TiO_2	Fresh	-	3.8	0.60
	1 cycle	-	2.9	1.48

* indicates that Pt or Cl are below the detection limit of the XPS measurement, 0.2×10^{-3} Pt/Ti or 0.02 at. % Cl.

† The high coverage of reactants/products leads to the low intensity of Pt.

Stability of Catalytic Performance and Post-Reaction Analysis

The stability of the supported metal center is a challenge, particularly in a solution-solid heterogeneous catalysis system. We examined stability by recovering the catalyst powder at the end of a reaction batch and then reusing it in subsequent reaction batch cycles. **Figure 9** shows that the Pt-DPTZ on defective TiO_2 (500 °C) catalyst has high activity for four cycles of batch reaction. When the same catalyst is used in a fresh batch reaction, the performance in the second reaction cycle is identical to the first (97% yield at 70 °C and 30 min for 2nd cycle vs 99% yield at 70 °C and 30 min for the 1st cycle), further indicating that the catalyst state before and after reaction is fairly similar. The catalyst reached 96% yield of product at the 3rd cycle and 91% yield of the product at the fourth cycle. The TON of reaction remains similar when compare the TON for the first cycle with the fourth cycle (**Table 4**).

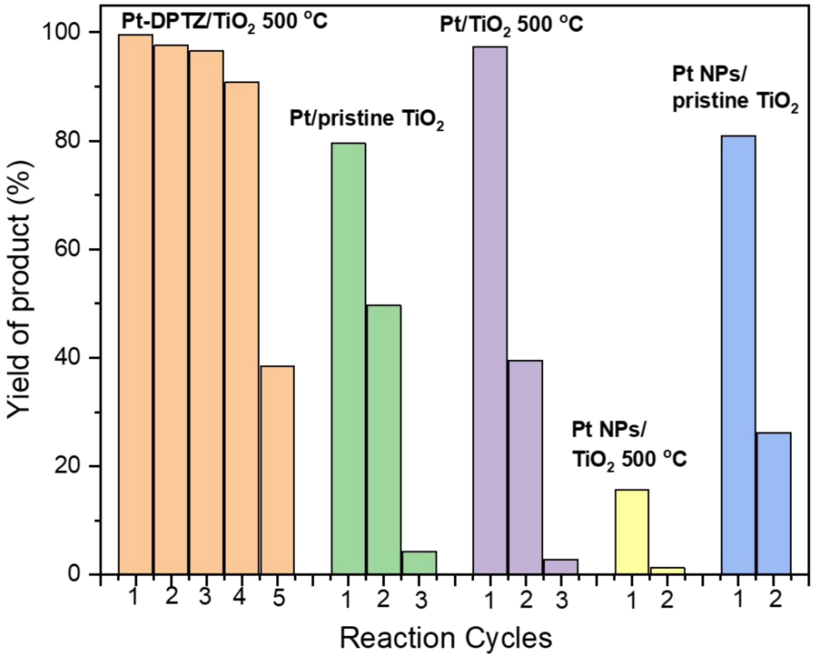

Figure 9. Reaction yield performance through multiple cycles of batch reaction by recycling the catalysts Pt-DPTZ/TiO_2 500 °C (orange), Pt/pristine TiO_2 (green), Pt/TiO_2 500 °C (purple), and reduced Pt nanoparticles on TiO_2 500 °C (yellow) and on pristine TiO_2 (blue). The yield of product is obtained at 70 °C for a reaction time of 30 min.

Table 4. Yield of hydrosilylation product and turnover number in the experiments of multiple cycles of batch reaction. These reactions were run at 70 °C for 30 min per cycle, but the data reported here are measured after 10 min reaction time, at which time full conversion of reactant silane is not yet reached for most of the catalysts, allowing for comparison of activity. ICP values are obtained *before* the reaction cycle indicated in the first column.

	Pt ratio (%, ICP-MS)	Yield of product (%)	TON
Pt-DPTZ/Pristine TiO_2 1st cycle	0.24	2.5	830
4th cycle	0.07	0	0
Pt-DPTZ/TiO_2 500 °C 1st cycle	0.63	99.2	12530
4th cycle	0.23	37.7	12440
Pt/TiO_2 1st cycle	0.42	75.1	12900
3rd cycle	0.03	3.4	7360
Pt/TiO_2 500 °C 1st cycle	0.55	92.5	12670
3rd cycle	0.08	1.9	2020
Pt NPs/TiO_2 1st cycle	1.00	32.2	3500
2nd cycle	0.30	0.4	127
Pt NPs/TiO_2 500 °C 1st cycle	1.00	2.1	184
2nd cycle	0.82	0.2	22

Role of ligand

To further examine the function of the organic ligand during the hydrosilylation reaction, a set of reference samples have been synthesized: bare Pt on pristine TiO_2 and on TiO_2 500 °C (STEM in **Figure 5e-5f**), reduced Pt nanoparticles (Ar/H_2 at 400 °C, TEM in **Figure S4**) on pristine TiO_2 and on TiO_2 500 °C.

The yield of the product after reaction at 70 °C for 30 min for each of these catalysts are shown in **Figure 9**. The fresh Pt-DPTZ on defective TiO_2 (500 °C anneal) and the bare Pt on defective TiO_2 (500 °C anneal) both show high activity in the first cycle. Although the coordination of bare Pt on defective TiO_2 may be less saturated than that of

Pt-DPTZ on defective TiO_2, the Pt-DPTZ/TiO_2 500 °C reaches a similar atom utilization efficiency with the supported bare Pt. Besides, both bare Pt and Pt-DPTZ species on defective TiO_2 are more active than supported Pt nanoparticles, because the nanoparticles are fully coordinated only the peripheral sites are actively open. For the supported Pt catalyst on TiO_2, the reaction follows the Chalk-Harrod mechanism, where the insertion of oct-1-ene to Pt-H bond occurs. Previous work[36] has shown the highest energy barrier in the reaction is the reduction elimination of Si-C, which is facilitated using isolated Pt atoms rather than Pt nanoparticles. This is in line with our findings: the most active species are the isolated Pt sites, instead of Pt nanoparticles or Pt clusters.

Additionally, the cyclic performances of the above reference catalysts are shown in **Figure 9**. For bare Pt deposited on pristine TiO_2 or on defective TiO_2 without ligand, the catalysts significantly lost the activity after one cycle of the experiments (97% yield of product at the first cycle and 40% yield of the product at the second cycle, performed at 70 °C for 30 min). **Table 4** shows a 40% drop in the TON for bare Pt on pristine TiO_2 at the third cycle of the reaction and 85% for bare Pt on defective TiO_2. For Pt NPs, a significant drop of the yield of the product has been detected in our experiment (**Figure 9**). The TON drops more than 98% at the second cycle for Pt NPs on pristine TiO_2 and 84% drop of TON for Pt NPs on defective TiO_2. However, Pt-DPTZ does not show a significant drop in activity in the second cycle, indicating that the ligand increases the stability of the metal center and does not hinder the reactivity of the Pt center.

Pt *4f* and Cl *2p* regions of XPS from supported Pt-ligand catalysts and reference samples are shown in **Figure S8-S9**. After three cycles of reaction at 70 °C for 30 min, the Pt loading for Pt-DPTZ on defective TiO_2 (500 °C anneal) remains to be 30%.

However, more than 90% of Pt detachment occurred from XPS after one cycle for bare Pt on pristine TiO_2 and defective TiO_2 (**Table 3**). ICP shows a loss of 70% Pt for Pt nanoparticles on the pristine TiO_2 surface, and 20% loss of Pt on the defective TiO_2 surface, after one cycle of reaction. XPS and ICP results both suggest that the bond between Pt and surface oxygen is not strong enough to preserve surface active Pt sites. Therefore, the presence of the DPTZ ligand stabilizes the single-atom Pt on the support to avoid leaching. We also note that because the Pt without ligand is readily leached from the surface in one reaction cycle (**Table 3**), non-complexed Pt would have to be only a small minority species on the Pt-DPTZ catalysts since the Pt intensity shows relatively little change under the same conditions.

The above results show the key advantages of Pt-ligand SACs over traditional metal nanoparticle catalysts: the high atom utilization efficiency, more uniform chemical environment, and higher durability during reaction. Compared to other methods to immobilize the Pt on the support,[74] the metal-ligand approach allows tuning of the metal properties. The comparison between these different Pt species (Pt-ligand, bare Pt and Pt NPs) on pristine TiO_2 or on defective TiO_2 strongly illustrates that both the metal-support and the metal-ligand interactions impact on the catalytic properties of Pt centers. This not only expands the understanding of metal-support interaction from nanoparticles to single-atoms, but also informs the design of appropriate forms of ligands for Pt to optimize the interactions.

Conclusions

In conclusion, defect-engineering of TiO_2 supports can alter the coordination environment of Pt single-atoms by affecting the degree of open coordination space for ligand binding while maintaining a consistent charged single-atom character of Pt. The modified coordination configuration improves the activity of metal-ligand single-atom Pt catalysts for hydrosilylation reactions compared with Pt single-atoms on pristine TiO_2, due to high dispersion of Pt-DPTZ single-atoms and a facile removal of chloride ligand in the reaction induction period. The metal-ligand approach of single-atom Pt enhances the durability of catalysts as well. These findings are of key importance when optimizing single-atom metal-ligand system for liquid phase heterogeneous catalysis. This oxide support defect engineering approach to improve SACs on high surface area supports can not only be further optimized to tune other TiO_2-supported catalysts, but can also be applied on other oxide support surfaces, especially ceria.

Associated content

The Supporting Information, including additional XP spectra, XRD patterns, Raman spectra, activation energy calculation of hydrosilylation reaction, EXAFS fitting parameters, XANES and TEM image, is available free of charge.

Corresponding Author

*E-mail: tait@indiana.edu.

ORCID

Xuemei Zhou: 0000-0002-3321-3606

Linxiao Chen: 0000-0003-3177-380X

George E. Sterbinsky: (none).

Debangshu Mukherjee: 0000-0003-0437-9807

Raymond R. Unocic: 0000-0002-1777-8228

Steven L. Tait: 0000-0001-8251-5232

Conflicts of Interest

There are no conflicts of interest to declare.

Acknowledgement

This work was supported by the U. S. Department of Energy, Office of Basic Energy Sciences, Chemical Sciences program, DE-SC0016367. XPS measurements were carried out at the Indiana University (IU) Nanoscale Characterization Facility, with assistance from Dr. Yaroslav Lasovyj. XAS measurements were performed at beamline 9-BM at the Advanced Photon Source, an Office of Science User Facility operated for the U.S. Department of Energy (DOE) Office of Science by Argonne National Laboratory, under Contract No. DE-AC02-06CH11357. Scanning transmission electron microscopy (STEM) and electron energy loss spectroscopy (EELS) measurements were performed at Center for Nanophase Materials Sciences, Oak Ridge National Laboratory, an Office of Science User Facility operated for the U.S. Department of Energy (DOE) Office of Science. GC-MS measurements were carried out at the IU Mass Spectrometry Facility, with assistance from

Dr. Jonathan A. Karty. ICP-MS measurements were performed in IU Department of Earth and Atmospheric Sciences by Benjamin Underwood. The authors thank Mackenzie Fahey for assistance with Raman spectroscopy measurements.

References

1. Schwab, G. M., Boundary-Layer Catalysis. *Angew. Chem. Int. Ed.* **1967**, *6*, 375-375.
2. Tauster, S. J.; Fung, S. C.; Garten, R. L., Strong Metal-Support Interactions. Group 8 Noble Metals Supported on TiO_2. *J. Am. Chem. Soc.* **1978**, *100*, 170-175.
3. Ro, I.; Resasco, J.; Christopher, P., Approaches for Understanding and Controlling Interfacial Effects in Oxide-Supported Metal Catalysts. *ACS Catal.* **2018**, *8*, 7368-7387.
4. Campbell, C. T., Electronic perturbations. *Nature Chemistry* **2012**, *4*, 597-598.
5. Tauster, S. J.; Fung, S. C.; Baker, R. T. K.; Horsley, J. A., Strong Interactions in Supported-Metal Catalysts. *Science* **1981**, *211*, 1121-1125.
6. Tauster, S. J., Strong metal-support interactions. *Acc. Chem. Res.* **1987**, *20*, 389-394.
7. Bahl, M. K.; Tsai, S. C.; Chung, Y. W., Auger and photoemission investigations of the platinum-$SrTiO_3$(100) interface: Relaxation and chemical-shift effects. *Phys. Rev. B* **1980**, *21*, 1344-1348.
8. Fu, Q.; Wagner, T., Interaction of nanostructured metal overlayers with oxide surfaces. *Surf Sci Rep.* **2007**, *62*, 431-498.
9. Zhou, Y.; Doronkin, D. E.; Chen, M.; Wei, S.; Grunwaldt, J.-D., Interplay of Pt and Crystal Facets of TiO_2: CO Oxidation Activity and Operando XAS/DRIFTS Studies. *ACS Catal.* **2016**, *6*, 7799-7809.
10. Gunasooriya, G. T. K. K.; Seebauer, E. G.; Saeys, M., Ethylene Hydrogenation over Pt/TiO_2: A Charge-Sensitive Reaction. *ACS Catal.* **2017**, *7*, 1966-1970.
11. Liu, L.; Corma, A., Metal Catalysts for Heterogeneous Catalysis: From Single Atoms to Nanoclusters and Nanoparticles. *Chem Rev* **2018**, *118*, 4981-5079.
12. Farmer, J. A.; Campbell, C. T., Ceria Maintains Smaller Metal Catalyst Particles by Strong Metal-Support Bonding. *Science* **2010**, *329*, 933-936.
13. Chen, Y.; Ji, S.; Chen, C.; Peng, Q.; Wang, D.; Li, Y., Single-Atom Catalysts: Synthetic Strategies and Electrochemical Applications. *Joule* **2018**, *2*, 1242-1264.
14. Yan, H.; Cheng, H.; Yi, H.; Lin, Y.; Yao, T.; Wang, C.; Li, J.; Wei, S.; Lu, J., Single-atom Pd1/graphene catalyst achieved by atomic layer deposition: remarkable performance in selective hydrogenation of 1, 3-butadiene. *J. Am. Chem. Soc.* **2015**, *137*, 10484-10487.

15. Wan, J.; Chen, W.; Jia, C.; Zheng, L.; Dong, J.; Zheng, X.; Wang, Y.; Yan, W.; Chen, C.; Peng, Q.; Wang, D.; Li, Y., Defect Effects on TiO_2 Nanosheets: Stabilizing Single Atomic Site Au and Promoting Catalytic Properties. *Adv. Mater.* **2018**, *30*, 1705369.

16. Kistler, J. D.; Chotigkrai, N.; Xu, P.; Enderle, B.; Praserthdam, P.; Chen, C.-Y.; Browning, N. D.; Gates, B. C., A Single-Site Platinum CO Oxidation Catalyst in Zeolite KLTL: Microscopic and Spectroscopic Determination of the Locations of the Platinum Atoms. *Angew. Chem. Int. Ed.* **2014**, *53*, 8904-8907.

17. DeRita, L.; Dai, S.; Lopez-Zepeda, K.; Pham, N.; Graham, G. W.; Pan, X.; Christopher, P., Catalyst Architecture for Stable Single Atom Dispersion Enables Site-Specific Spectroscopic and Reactivity Measurements of CO Adsorbed to Pt Atoms, Oxidized Pt Clusters, and Metallic Pt Clusters on TiO2. *J Am Chem Soc* **2017**, *139*, 14150-14165.

18. Kyriakou, G.; Boucher, M. B.; Jewell, A. D.; Lewis, E. A.; Lawton, T. J.; Baber, A. E.; Tierney, H. L.; Flytzani-Stephanopoulos, M.; Sykes, E. C. H., Isolated Metal Atom Geometries as a Strategy for Selective Heterogeneous Hydrogenations. *Science* **2012**, *335*, 1209-1212.

19. Fu, Q.; Saltsburg, H.; Flytzani-Stephanopoulos, M., Active Nonmetallic Au and Pt Species on Ceria-Based Water-Gas Shift Catalysts. *Science* **2003**, *301*, 935.

20. Cao, S.; Yang, M.; Elnabawy, A. O.; Trimpalis, A.; Li, S.; Wang, C.; Göltl, F.; Chen, Z.; Liu, J.; Shan, J.; Li, M.; Haas, T.; Chapman, K. W.; Lee, S.; Allard, L. F.; Mavrikakis, M.; Flytzani-Stephanopoulos, M., Single-atom gold oxo-clusters prepared in alkaline solutions catalyse the heterogeneous methanol self-coupling reactions. *Nature Chemistry* **2019**, *11*, 1098-1105.

21. Copéret, C.; Chabanas, M.; Petroff Saint-Arroman, R.; Basset, J.-M., Homogeneous and Heterogeneous Catalysis: Bridging the Gap through Surface Organometallic Chemistry. *Angew. Chem. Int. Ed.* **2003**, *42*, 156-181.

22. Samantaray, M. K.; D'Elia, V.; Pump, E.; Falivene, L.; Harb, M.; Ould Chikh, S.; Cavallo, L.; Basset, J.-M., The Comparison between Single Atom Catalysis and Surface Organometallic Catalysis. *Chemical Reviews* **2019**.

23. Tempas, C. D.; Morris, T.; Wisman, D. L.; Le, D.; Din, N. U.; Williams, C. G.; Wang, M.; Polezhaev, A. V.; Rahman, T. S.; Caulton, K. G.; Tait, S. L., Redox-active ligand controlled selectivity of vanadium oxidation on Au(100). *Chem. Sci.* **2018**, *9*, 1674-1685.

24. Chen, L.; Sterbinsky, G. E.; Tait, S. L., Synthesis of platinum single-site centers through metal-ligand self-assembly on powdered metal oxide supports. *J. Catal.* **2018**, *365*, 303-312.

25. Skomski, D.; Tempas, C. D.; Cook, B. J.; Polezhaev, A. V.; Smith, K. A.; Caulton, K. G.; Tait, S. L., Two and Three Electron Oxidation of Single-site Vanadium Centers at Surfaces by Ligand Design. *J. Am. Chem. Soc.* **2015**, *137*, 7898-7902.

26. Skomski, D.; Tempas, C. D.; Smith, K. A.; Tait, S. L., Redox-Active On-Surface Assembly of Metal-Organic Chains with Single-Site Pt(II). *J. Am. Chem. Soc.* **2014**, *136*, 9862-9865.

27. Chen, L.; Ali, I. S.; Sterbinsky, G. E.; Gamler, J. T. L.; Skrabalak, S. E.; Tait, S. L., Alkene Hydrosilylation on Oxide-Supported Pt-Ligand Single-Site Catalysts. *ChemCatChem* **2019**, *11*, 2843-2854.

28. Meister, T. K.; Riener, K.; Gigler, P.; Stohrer, J.; Herrmann, W. A.; Kühn, F. E., Platinum Catalysis Revisited—Unraveling Principles of Catalytic Olefin Hydrosilylation. *ACS Catal.* **2016**, *6*, 1274-1284.

29. Nakajima, Y.; Shimada, S., Hydrosilylation reaction of olefins: recent advances and perspectives. *RSC Adv.* **2015**, *5*, 20603-20616.

30. Marciniec, B.; Guliński, J., Recent advances in catalytic hydrosilylation. *J. Org. Chem.* **1993**, *446*, 15-23.

31. Lewis, L. N.; Sy, K. G.; Bryant Jr, G. L.; Donahue, P. E., Platinum-catalyzed hydrosilylation of alkynes. *Organometallics* **1991**, *10*, 3750-3759.

32. Hofmann, J. R.; Vlatković, M.; Wiesbrock, F., Fifty Years of Hydrosilylation in Polymer Science: A Review of Current Trends of Low-Cost Transition-Metal and Metal-Free Catalysts, Non-Thermally Triggered Hydrosilylation Reactions, and Industrial Applications. *Polymers* **2017**, *9*, 534.

33. Maciejewski, H.; Wawrzyńczak, A.; Dutkiewicz, M.; Fiedorow, R., Silicone waxes—synthesis via hydrosilylation in homo-and heterogeneous systems. *Journal of Molecular Catalysis A: Chemical* **2006**, *257*, 141-148.

34. Cui, X.; Junge, K.; Dai, X.; Kreyenschulte, C.; Pohl, M.-M.; Wohlrab, S.; Shi, F.; Brückner, A.; Beller, M., Synthesis of Single Atom Based Heterogeneous Platinum

Catalysts: High Selectivity and Activity for Hydrosilylation Reactions. *ACS Cent. Sci.* **2017**, *3*, 580-585.

35. Zhang, Z.; Bai, L.; Hu, X., Alkene hydrosilylation catalyzed by easily assembled Ni(ii)-carboxylate MOFs. *Chemical Science* **2019**, *10*, 3791-3795.

36. Chen, Y.; Ji, S.; Sun, W.; Chen, W.; Dong, J.; Wen, J.; Zhang, J.; Li, Z.; Zheng, L.; Chen, C.; Peng, Q.; Wang, D.; Li, Y., Discovering Partially Charged Single-Atom Pt for Enhanced Anti-Markovnikov Alkene Hydrosilylation. *J. Am. Chem. Soc.* **2018**, *140*, 7407-7410.

37. Zhou, X.; Liu, N.; Schmuki, P., Photocatalysis with TiO_2 Nanotubes: “Colorful” Reactivity and Designing Site-Specific Photocatalytic Centers into TiO_2 Nanotubes. *ACS Catal.* **2017**, *7*, 3210-3235.

38. Haruta, M., Size- and support-dependency in the catalysis of gold. *Catal. Today* **1997**, *36*, 153-166.

39. Haruta, M.; Tsubota, S.; Kobayashi, T.; Kageyama, H.; Genet, M. J.; Delmon, B., Low-Temperature Oxidation of CO over Gold Supported on TiO_2, α-Fe_2O_3, and Co_3O_4. *J. Catal.* **1993**, *144*, 175-192.

40. Fujishima, A.; Zhang, X.; Tryk, D. A., TiO_2 photocatalysis and related surface phenomena. *Surf. Sci. Rep.* **2008**, *63*, 515-582.

41. Li, H.; Guo, Y.; Robertson, J., Calculation of TiO_2 Surface and Subsurface Oxygen Vacancy by the Screened Exchange Functional. *J. Phys. Chem. C* **2015**, *119*, 18160-18166.

42. Morita, K.; Yasuoka, K., Density functional theory study of atomic and electronic properties of defects in reduced anatase TiO_2 nanocrystals. *AIP Advances* **2018**, *8*, 035119.

43. Setvin, M.; Franchini, C.; Hao, X.; Schmid, M.; Janotti, A.; Kaltak, M.; Van de Walle, C. G.; Kresse, G.; Diebold, U., Direct View at Excess Electrons in TiO2 Rutile and Anatase. *Phys. Rev. Lett.* **2014**, *113*, 086402.

44. Chen, X.; Liu, L.; Yu, P. Y.; Mao, S. S., Increasing solar absorption for photocatalysis with black hydrogenated titanium dioxide nanocrystals. *Science* **2011**, *331*, 746-750.

45. Zheng, Z.; Huang, B.; Lu, J.; Wang, Z.; Qin, X.; Zhang, X.; Dai, Y.; Whangbo, M.-H., Hydrogenated titania: synergy of surface modification and morphology improvement for enhanced photocatalytic activity. *Chem. Commun.* **2012**, *48*, 5733-5735.

46. Scheiber, P.; Fidler, M.; Dulub, O.; Schmid, M.; Diebold, U.; Hou, W.; Aschauer, U.; Selloni, A., (Sub)Surface Mobility of Oxygen Vacancies at the TiO2 Anatase (101) Surface. *Phys. Rev. Lett.* **2012**, *109*, 136103.

47. Liu, X.; Zhu, G.; Wang, X.; Yuan, X.; Lin, T.; Huang, F., Progress in Black Titania: A New Material for Advanced Photocatalysis. *Adv. Energy Mater.* **2016**, *6*, 1600452.

48. Zhou, X.; Liu, N.; Schmuki, P., Ar+-ion bombardment of TiO2 nanotubes creates co-catalytic effect for photocatalytic open circuit hydrogen evolution. *Electrochem. Commun.* **2014**, *49*, 60-64.

49. Liu, X.; Zhu, G.; Wang, X.; Yuan, X.; Lin, T.; Huang, F., Progress in Black Titania: A New Material for Advanced Photocatalysis. *Advanced Energy Materials* **2016**, *6*, 1600452.

50. Chen, X.; Liu, L.; Yu, P. Y.; Mao, S. S., Increasing Solar Absorption for Photocatalysis with Black Hydrogenated Titanium Dioxide Nanocrystals. *Science* **2011**, *331*, 746.

51. Cueva, P.; Hovden, R.; Mundy, J. A.; Xin, H. L.; Muller, D. A., Data Processing for Atomic Resolution Electron Energy Loss Spectroscopy. *Microsc. Microanal.* **2012**, *18*, 667-675.

52. Ravel, B.; Newville, M., ATHENA, ARTEMIS, HEPHAESTUS: data analysis for X-ray absorption spectroscopy using IFEFFIT. *J. Synchrotron Radiat.* **2005**, *12*, 537-541.

53. He, H.; Yang, K.; Wang, N.; Luo, F.; Chen, H., Hydrogenated TiO_2 film for enhancing photovoltaic properties of solar cells and self-sensitized effect. *J. Appl. Phys.* **2013**, *114*, 213505.

54. Chiesa, M.; Paganini, M. C.; Livraghi, S.; Giamello, E., Charge trapping in TiO_2 polymorphs as seen by Electron Paramagnetic Resonance spectroscopy. *Phys. Chem. Chem. Phys.* **2013**, *15*, 9435-9447.

55. Livraghi, S.; Chiesa, M.; Paganini, M. C.; Giamello, E., On the Nature of Reduced States in Titanium Dioxide As Monitored by Electron Paramagnetic Resonance. I: The Anatase Case. *J. Phys. Chem. C* **2011**, *115*, 25413-25421.

56. Weckhuysen, B. M.; Heidler, R.; Schoonheydt, R. a., Electron Spin Resonance Spectroscopy. *Mol. Sieves* **2004**, *4*, 295-335.

57. Brckner, A., In situ electron paramagnetic resonance: a unique tool for analyzing structure-reactivity relationships in heterogeneous catalysis. *Chem. Soc. Rev.* **2010**, *39*, 4673-4684.

58. Berger, T.; Sterrer, M.; Diwald, O.; Knzinger, E., Charge trapping and photoadsorption of O_2 on dehydroxylated TiO_2 nanocrystals - An electron paramagnetic resonance study. *ChemPhysChem* **2005**, *6*, 2104-2112.

59. Zhou, X.; Liu, N.; Schmidt, J.; Kahnt, A.; Osvet, A.; Romeis, S.; Zolnhofer, E. M.; Marthala, V. R. R.; Guldi, D. M.; Peukert, W.; Hartmann, M.; Meyer, K.; Schmuki, P., Noble-Metal-Free Photocatalytic Hydrogen Evolution Activity: The Impact of Ball Milling Anatase Nanopowders with TiH_2. *Adv. Mater.* **2017**, *29*, 1604747.

60. Liu, N.; Zhou, X.; Nguyen, N. T.; Peters, K.; Zoller, F.; Hwang, I.; Schneider, C.; Miehlich, M. E.; Freitag, D.; Meyer, K.; Fattakhova-Rohlfing, D.; Schmuki, P., Black Magic in Gray Titania: Noble-Metal-Free Photocatalytic H_2 Evolution from Hydrogenated Anatase. *ChemSusChem* **2017**, *10*, 62-67.

61. Xing, M.; Li, X.; Zhang, J., Synergistic effect on the visible light activity of Ti3+ doped TiO2 nanorods/boron doped graphene composite. *Scientific Reports* **2014**, *4*, 5493.

62. Livraghi, S.; Paganini, M. C.; Giamello, E.; Selloni, A.; Valentin, C. D.; Pacchioni, G., Origin of Photoactivity of Nitrogen-Doped Titanium Dioxide under Visible Light Origin of Photoactivity of Nitrogen-Doped Titanium Dioxide under Visible Light. *J. Am. Chem. Soc.* **2006**, *128*, 15666-15671.

63. Duan, M.-Y.; Li, J.; Li, M.; Zhang, Z.-Q.; Wang, C., Pt(II) porphyrin modified TiO_2 composites as photocatalysts for efficient 4-NP degradation. *Appl. Surf. Sci.* **2012**, *258*, 5499-5504.

64. Tempas, C. D.; Skomski, D.; Cook, B. J.; Le, D.; Smith, K. A.; Rahman, T. S.; Caulton, K. G.; Tait, S. L., Redox Isomeric Surface Structures Are Preferred over Odd-Electron Pt(1). *Chem.: Eur. J.* **2018**, *24*, 15852-15858.

65. Qiao, B.; Wang, A.; Yang, X.; Allard, L. F.; Jiang, Z.; Cui, Y.; Liu, J.; Li, J.; Zhang, T., Single-atom catalysis of CO oxidation using Pt1/FeOx. *Nature chemistry* **2011**, *3*, 634-641.

66. Resasco, J.; DeRita, L.; Dai, S.; Chada, J. P.; Xu, M.; Yan, X.; Finzel, J.; Hanukovich, S.; Hoffman, A. S.; Graham, G. W.; Bare, S. R.; Pan, X.; Christopher, P., Uniformity Is

Key in Defining Structure–Function Relationships for Atomically Dispersed Metal Catalysts: The Case of Pt/CeO2. *J. Am. Chem. Soc.* **2020**, *142*, 169-184.

67. Gates, B. C., Atomically Dispersed Supported Metal Catalysts: Seeing Is Believing. *Trends in Chemistry* **2019**, *1*, 99-110.

68. DeRita, L.; Resasco, J.; Dai, S.; Boubnov, A.; Thang, H. V.; Hoffman, A. S.; Ro, I.; Graham, G. W.; Bare, S. R.; Pacchioni, G.; Pan, X.; Christopher, P., Structural evolution of atomically dispersed Pt catalysts dictates reactivity. *Nature Materials* **2019**, *18*, 746-751.

69. Harrod, J. F.; Chalk, A. J., Homogeneous Catalysis. I. Double Bond Migration in n-Olefins, Catalyzed by Group VIII Metal Complexes. *J. Am. Chem. Soc.* **1964**, *86*, 1776-1779.

70. Marciniec, B., Catalysis by transition metal complexes of alkene silylation–recent progress and mechanistic implications. *Coordination Chemistry Reviews* **2005**, *249*, 2374-2390.

71. Hadjiivanov, K. I., IR study of CO and H_2O coadsorption on Pt^+/TiO_2 and Pt/TiO_2 samples. *J. Chem. Soc. Faraday Trans.* **1998**, *94*, 1901-1904.

72. Kalhara Gunasooriya, G. T. K.; Saeys, M., CO Adsorption Site Preference on Platinum: Charge Is the Essence. *ACS Catal.* **2018**, *8*, 3770-3774.

73. Thang, H. V.; Pacchioni, G.; DeRita, L.; Christopher, P., Nature of stable single atom Pt catalysts dispersed on anatase TiO2. *J. Catal.* **2018**, *367*, 104-114.

74. Galeandro-Diamant, T.; Sayah, R.; Zanota, M.-L.; Marrot, S.; Veyre, L.; Thieuleux, C.; Meille, V., Pt nanoparticles immobilized in mesostructured silica: a non-leaching catalyst for 1-octene hydrosilylation. *Chem. Commun.* **2017**, *53*, 2962-2965.

Pt-ligand Single-atom Catalysts: Tuning Activity by Oxide Support Defect Density

Xuemei Zhou,[a] Linxiao Chen,[a] George E. Sterbinsky,[b] Debangshu Mukherjee,[c]

*Raymond R. Unocic,[c] Steven L. Tait[a]**

Table of Contents Entry

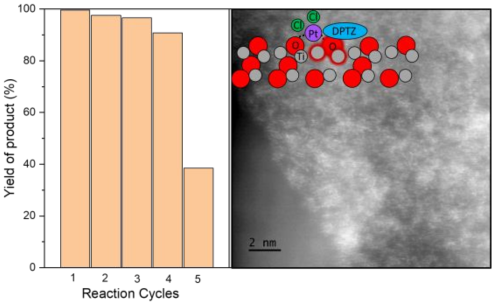

Metal-ligand coordination stabilizes single atom Pt on pristine and defective TiO_2 supports to impact local coordination and catalytic hydrosilylation activity.